J. Fluid Mech. (2006), *vol.* 561, *pp.* 255–277.
doi:10.1017/S0022112006000681 Printed in the United Kingdom

Onset of three-dimensional unsteady states in small-aspect-ratio Taylor–Couette flow

By F. MARQUES[1] AND J. M. LOPEZ[2]

[1]Departament de Física Aplicada, Univ. Politècnica de Catalunya, Barcelona 08034, Spain
[2]Department of Mathematics and Statistics, Arizona State University, Tempe, AZ 85287, USA

(Received 9 November 2005 and in revised form 12 January 2006)

A numerical investigation of the onset of three-dimensional states in Taylor–Couette flow for aspect ratio one is presented. Two main branches exist, one preserving and the other breaking the reflection symmetry about the mid-plane. Both branches become three-dimensional via Hopf bifurcations to rotating waves with different azimuthal wavenumbers. Moreover, the symmetric branch exhibits secondary Hopf bifurcations and transitions to complex spatio-temporal dynamics at Reynolds numbers $Re \sim 1000$. The analysis of the three-dimensional solutions shows that the dynamics is driven by the jet of angular momentum erupting from the inner cylinder boundary layer and its interactions with the sidewall and endwall layers. The various solutions are organized by a lattice of spatial and spatio-temporal symmetry subgroups which provides a framework for the relationships between the solution types and for the symmetry-breaking bifurcations. The results obtained agree with previous experimental results and help clarify many aspects of the mode competition at the higher Re values.

1. Introduction

The flow between two concentric cylinders driven by their differential rotation, Taylor–Couette flow, has played a central role in the development of hydrodynamic stability theory (Taylor 1923). Its geometric simplicity allows well-controlled experiments which may shed light on the transition to hydrodynamic turbulence. Theoretical progress originally proceeded by making two geometric idealizations: (i) that the height-to-gap aspect ratio of the annulus $\Gamma \to \infty$, and (ii) that the radius ratio of the two cylinders $\eta \to 1$, i.e. infinite cylinders and narrow gap approximations. The simplifications in the mathematical description of the problem due to these geometric idealizations are that in the limit $\eta \to 1$, curvature effects are negligible. The limit $\Gamma \to \infty$, together with the assumption of periodicity in the axial z-direction leads to a (unique) basic state that is a function only of r, specified by the radii and the non-dimensional rotation rates of the cylinders (i.e. Reynolds numbers). Under these idealizations, the system is invariant to both reflection about any height z and translations in z ($O(2)$ symmetry), and arbitrary rotations about the axis ($SO(2)$ symmetry). Nevertheless, the limit $\Gamma \to \infty$ is singular, and endwall effects are not negligible even in very long Taylor–Couette systems (Benjamin 1978*a*, *b*; Lorenzen & Mullin 1985; Cliffe, Kobine & Mullin 1992). The presence of endwalls, even in the limit of being infinitely far apart, completely destroys the translation invariance of the $O(2)$ symmetry in the idealized theory. In any physical Taylor–Couette system in which the two endwalls are both stationary or both rotating at the same rate, the

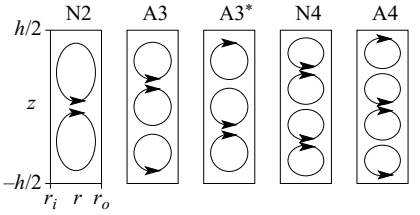

FIGURE 1. Solutions with different numbers of Taylor cells. Arrows indicate the outgoing jets. The flow at the endwalls moves inward for normal modes N2 and N4, and outward for anomalous modes A3, A3* and A4. The schematics show a meridonal section ($\theta =$ constant), $r = r_i$ and $r = r_o$ are the inner and outer cylinder radii and the endwalls are at $z = \pm h/2$.

symmetry of the problem (ignoring any small imperfections) is $SO(2) \times Z_2$, consisting of rotations about the axis and a reflection about the cylinder half-height.

A direct consequence of destroying the continuous translation symmetry by the presence of endwalls is that instead of a continuous spectrum in axial wavenumber, the system has a discrete spectrum in z, and the basic state is a function of (r, z). Instability is still, primarily, centrifugal in nature, owing to the rotating inner cylinder introducing a large negative radial gradient of angular momentum into the flow. The flow tends to redistribute the angular momentum via viscous diffusion if the flow inertia is sufficiently small, or by nonlinear advection for larger flow inertia. When the outer cylinder is at rest, which is the case considered in this paper, the nonlinear advection of angular momentum is accomplished by the eruption of jets of angular momentum from the boundary layer on the rotating inner cylinder, which generally lead to the formation of counter-rotating cells about the jets – known as Taylor vortices. These vortices tend to have unit aspect ratio in (r, z) when the endwalls are far apart, but for short annuli the cells can be quite far from unit aspect ratio.

For a physical apparatus, the endwalls are non-slip and Γ is finite. For endwalls at rest, the endwall boundary layer flow tends to be radially inward; on increasing Re from small values, weak Taylor-like cells appear close to the endwalls that become stronger and eventually fill the gap between the cylinders in a smooth process resulting in cellular flow with radial inflow at the endwalls. Figure 1 depicts examples of these so-called normal modes with radial inflow at the boundaries, N2 with two cells and N4 with four cells. The cellular flows with radial outflow at the boundaries are disconnected branches, the so-called anomalous cases (Benjamin 1978*a*, *b*; Benjamin & Mullin 1981). The solutions A3, A3* and A4 in figure 1 depict anomalous modes with three and four cells. The flows N2, N4, and A4 are Z_2-invariant, and A3 and A3* are symmetrically related.

For a given finite Γ, one of the normal cellular flows is smoothly connected with the Stokes flow solution at $Re \to 0$. The normal modes, being Z_2-invariant, have an even number of cells. As the more stable cells tend to be square, for the case shown schematically in figure 1 with $\Gamma \sim 4$, the flow smoothly connected with the Stokes flow solution is N4. The other states appear at higher Re via the following types of bifurcations. The Z_2-symmetric cellular flows, such as N2 and A4, appear in saddle-node bifurcations, as shown in figure 2(*a*). The flows with broken Z_2-symmetry appear via pitchfork bifurcations, as illustrated in figure 2(*b*); the pitchfork bifurcation may be supercritical (left) or subcritical (right). In the subcritical case, a pair of saddle-node bifurcations occurs simultaneously at a critical Re. For some Γ, the subcritical

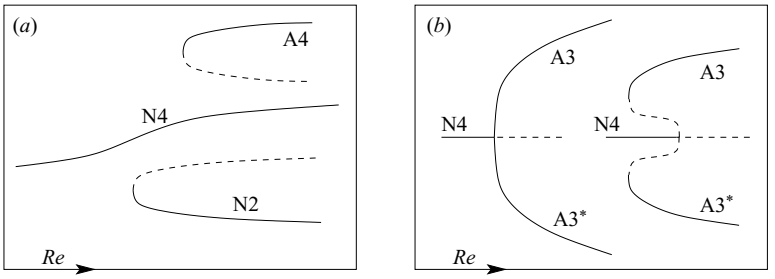

FIGURE 2. Possible bifurcations for finite Γ. In (a) the bifurcations take place in a Z_2-invariant subspace, and in (b) the bifurcations break the Z_2-symmetry.

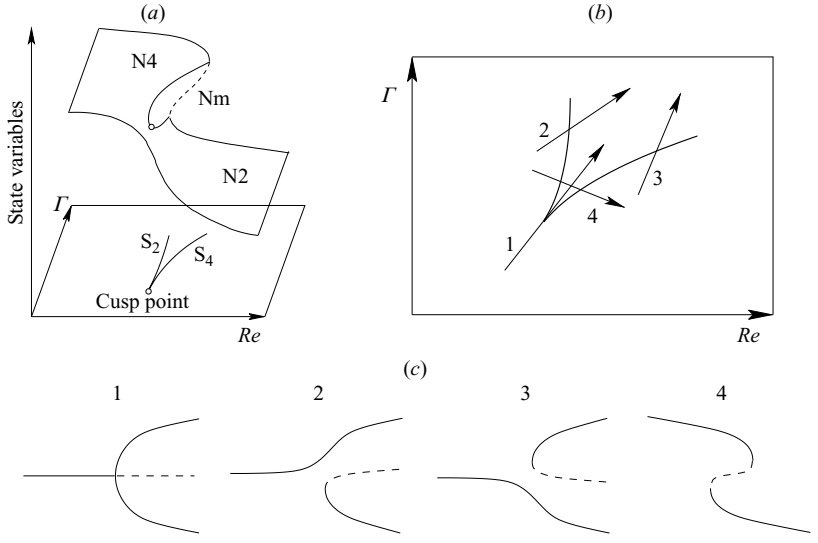

FIGURE 3. (a) Schematic of the cusp bifurcation, (b) one-parameter paths near the cusp bifurcation, and (c) bifurcations along the one-parameter paths in (b).

pitchfork bifurcation occurs at $Re \to \infty$, leaving a pair of simultaneous saddle-node bifurcations that do not connect with the symmetric branch N4.

As Γ is varied, the number and type of bifurcations change, as do their relative ordering with respect to Re. A relevant case is when the branch smoothly connected with the Stokes flow changes. For example, if we reduce Γ in figure 1, then for sufficiently small Γ the cellular flow connected with the trivial solution changes from N4 to N2. Figure 3 shows schematically the competition between the two modes, which is organized by a codimension-two cusp bifurcation (figure 3a). Figure 3(b) shows several one-parameter paths near the cusp and figure 3(c) shows schematics of the bifurcations along these one-parameter paths. Path 1, through the cusp point and tangent to the cusp, is identical to a pitchfork bifurcation. Paths 2 and 3 show the two possible unfoldings, where either the N2 or the N4 state remains continuously connected with the Stokes flow. Path 4 shows the relationship between the two saddle-node bifurcations, connected via an unstable intermediate state, Nm in figure 3(a). A pitchfork due to symmetry breaking is a codimension-one bifurcation, located by varying only one parameter. The codimension-two pitchfork corresponding to path 1 is not associated with any symmetry, and must necessarily be part of a codimension-two

bifurcation that includes the unfolding of the pitchfork, as in the case of the cusp bifurcation. This scenario is typical for moderate to large aspect ratios, $\Gamma \gtrsim 3$.

For small Γ, anomalous modes with a small number of cells bifurcate at low Re and the competition between these and the normal modes leads to very rich dynamics. For $\Gamma \sim 1$, the competition is between A1 and N2. The low-Re regime, where the flows remain steady and axisymmetric, has been extensively studied over the past quarter-century (Benjamin & Mullin 1981; Cliffe 1983; Pfister *et al.* 1988; Pfister, Schulz & Lensch 1991; Pfister, Buzug & Enge 1992) and a comprehensive understanding of the dynamics involved has emerged (Mullin *et al.* 2002). Some solutions leading to time-periodic flow have also been found when the Navier–Stokes equations are restricted to being axisymmetric (Furukawa *et al.* 2002). However, at moderate to large Re ($Re > 800$), the flows are unstable to non-axisymmetric perturbations. As noted in Mullin *et al.* (2002): "Time dependence and disorder is observed in the flow at higher Re, but an understanding of its evolution remains an outstanding challenge." Here, we provide a systematic study of the transition to spatio-temporal complexity using direct numerical simulations of the three-dimensional Navier–Stokes equations. We consider a one-parameter path of increasing Re while the aspect ratio and radius ratio are fixed at $\Gamma = 1.0$ and $\eta = 0.5$. This path cuts through the heart of the competition between A1 and N2, where for $Re > 850$ multiple bifurcations of these states have been observed experimentally (Pfister *et al.* 1991, 1992). The three-dimensional numerical solutions show that the manner in which the jet of angular momentum erupting from the inner cylinder boundary layer behaves, as it redistributes the angular momentum and its interactions with the sidewall and endwall boundary layers, leads to the various spatio-temporal states which break various aspects of the symmetry of the problem.

2. Navier–Stokes equations and the numerical scheme

Consider the flow in an annular region with inner radius r_i and outer radius r_o, capped by endwalls a distance h apart. The endwalls and the outer cylinder are stationary, and the flow is driven by the rotation of the inner cylinder at constant angular speed Ω. To non-dimensionalize the system, the annular gap $d = r_o - r_i$ is used as the length scale, and the time scale is the viscous time d^2/ν, where ν is the kinematic viscosity of the fluid. The system is governed by two geometric parameters and one dynamic parameter:

$$\begin{array}{ll} \text{radius ratio:} & \eta = r_i/r_o, \\ \text{aspect ratio:} & \Gamma = h/d, \\ \text{Reynolds number:} & Re = \Omega r_i d/\nu. \end{array}$$

Throughout this study, we shall keep the geometry fixed at $\Gamma = 1$ and $\eta = 0.5$ and vary Re. Figure 4 shows a schematic of the flow.

In cylindrical coordinates, (r, θ, z), the non-dimensional velocity vector and pressure are denoted by $\boldsymbol{u} = (u, v, w)$ and p, respectively. The governing equations are the (non-dimensional) Navier–Stokes equations

$$\left.\begin{array}{l} \partial \boldsymbol{u}/\partial t + (\boldsymbol{u}\cdot\nabla)\boldsymbol{u} = -\nabla p + \nabla^2 \boldsymbol{u}, \\ \nabla\cdot\boldsymbol{u} = 0, \end{array}\right\} \tag{2.1}$$

subject to no-slip boundary conditions. Specifically, u, v, and w are zero on all stationary boundaries, i.e. at the outer cylinder, $r = r_o/d = 1/(1-\eta) = 2$, and the top and

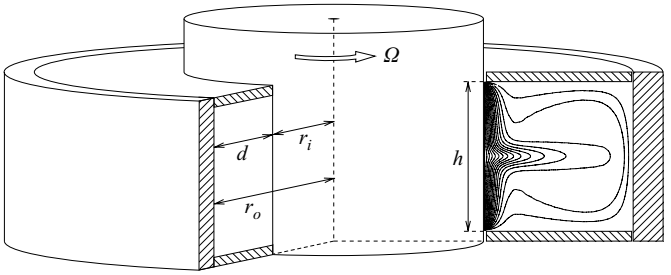

FIGURE 4. Schematic of the flow apparatus.

bottom endwalls $z = \pm 0.5h/d = \pm 0.5\Gamma$. On the rotating inner cylinder, $r = r_i/d = \eta/(1-\eta) = 1$, u and w are zero and $v = Re$.

To solve (2.1), a stiffly stable semi-implicit second-order projection scheme is used, where the linear terms are treated implicitly while the nonlinear terms are explicit. For the space variables, we use a Legendre–Fourier approximation (Lopez & Shen 1998; Lopez, Marques & Shen 2002) The spectral convergence of the code has already been extensively described for related problems (Lopez & Marques 2003; Lopez, Marques & Shen 2004; Abshagen *et al.* 2005*a*, *b*; Lopez & Marques 2005). The results presented here have 48 Legendre modes in the radial and axial directions, respectively, and up to 48 Fourier modes in θ (resolving up to azimuthal wavenumber $m = 24$); the time-step used is $\delta t = 2 \times 10^{-5}$.

One global measure we have used to characterize the various solutions obtained is the (scaled) kinetic energy in the mth Fourier mode of the solution:

$$E_m = \frac{1}{2Re^2} \int_{z=-\Gamma/2}^{z=\Gamma/2} \int_{r=1}^{r=2} \boldsymbol{u}_m \cdot \overline{\boldsymbol{u}}_m r \, \mathrm{d}r \, \mathrm{d}z, \tag{2.2}$$

where $\boldsymbol{u}_m$ is the mth Fourier mode of the velocity field. For oscillatory states where E_m is time-dependent, we use the time average $\langle E_m \rangle$ and the oscillation amplitude ΔE_m as characteristics.

3. Axisymmetric states and bifurcations

We begin with a brief summary of the A1–N2 mode competition for $Re < 750$. This has been extensively studied previously (see references in the Introduction), and is presented here to provide context for the new results at higher Re. Figure 5 is a bifurcation diagram with Re for $\Gamma = 1$ and $\eta = 0.5$, showing all the stable solution branches (curves with filled symbols) we have found, as well as the extension of some of these when the solutions lose stability at Hopf or pitchfork bifurcations (curves with open symbols).

The solution that is smoothly connected to the Stokes flow (at $Re \to 0$) is the two-cell normal mode N2. N2 has full symmetry; it is steady, axisymmetric and reflection symmetric. The actions of these invariances on any solution $\boldsymbol{U} = (u, v, w)(r, \theta, z, t)$ are

$$\text{time translations:} \quad \Phi_\tau(u, v, w)(r, \theta, z, t) = (u, v, w)(r, \theta, z, t + \tau), \quad \tau \in \mathbb{R}, \tag{3.1}$$

$$\text{rotations:} \quad R_\alpha(u, v, w)(r, \theta, z, t) = (u, v, w)(r, \theta + \alpha, z, t), \quad \alpha \in [0, 2\pi), \tag{3.2}$$

$$\text{reflection:} \quad K(u, v, w)(r, \theta, z, t) = (u, v, -w)(r, \theta, -z, t). \tag{3.3}$$

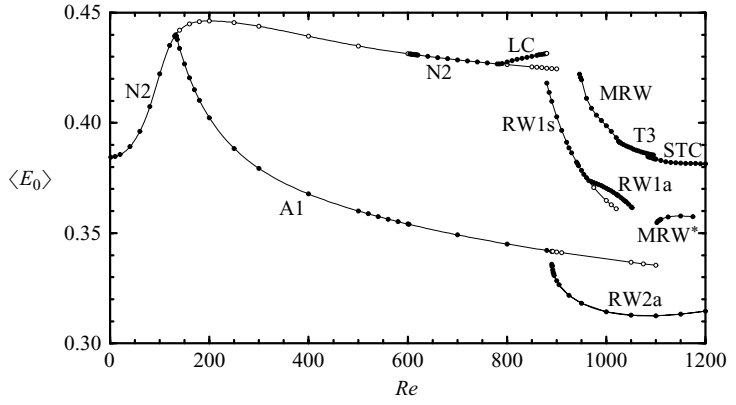

FIGURE 5. Bifurcation diagram with Re for $\Gamma = 1$ and $\eta = 0.5$, using $\langle E_0 \rangle$ as the measure of the flow state. States on solution curves with filled (open) symbols are stable (unstable).

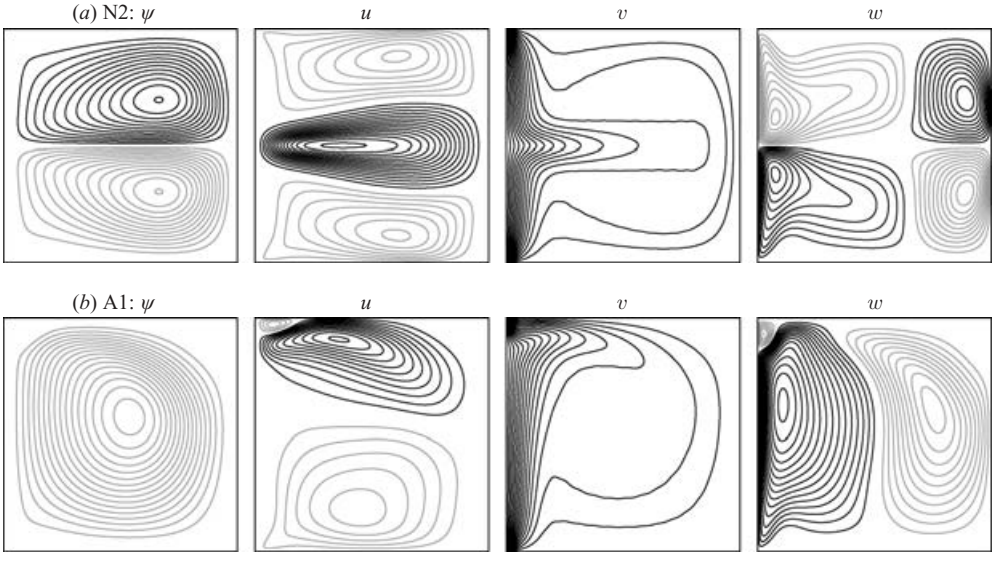

FIGURE 6. Contours of the streamfunction and velocity components of (*a*) N2 and (*b*) A1, both at $Re = 700$. There are 16 positive (black) and 16 negative (grey) linearly spaced contour levels in the ranges (*a*) $\psi \in [-20, 20]$, (*b*) $u \in [-160, 160]$, (*c*) $v \in [0, Re]$, (*d*) $w \in [-90, 90]$.

Since the aspect ratio $\Gamma = 1$, the cells are not square but severely compressed in z, and this solution loses stability at $Re \approx 133$ in a pitchfork bifurcation to the one-cell states A1 and A1* (they both have the same E_0), breaking the Z_2 symmetry. An A1 solution $\boldsymbol{U}_{A1}$ is such that $\Phi_\tau \boldsymbol{U}_{A1} = \boldsymbol{U}_{A1}$, $R_\alpha \boldsymbol{U}_{A1} = \boldsymbol{U}_{A1}$, and $K\boldsymbol{U}_{A1} = \boldsymbol{U}_{A1^*}$. These two symmetrically related states are stable up to $Re \approx 892$. N2 restabilizes in a second pitchfork bifurcation at $Re \approx 603$ and the bifurcated states are unstable. The experimental results in Pfister *et al.* (1988) report this to occur at $Re \approx 610$. Both N2 and A1 coexist and are stable in the range $Re \in [603, 786]$; evolution to one or the other state depends on initial conditions.

Figure 6(*a*) shows contours of the streamfunction and velocity components of N2 at $Re = 700$. The swirling jet of outgoing fluid is clearly evident in the contours

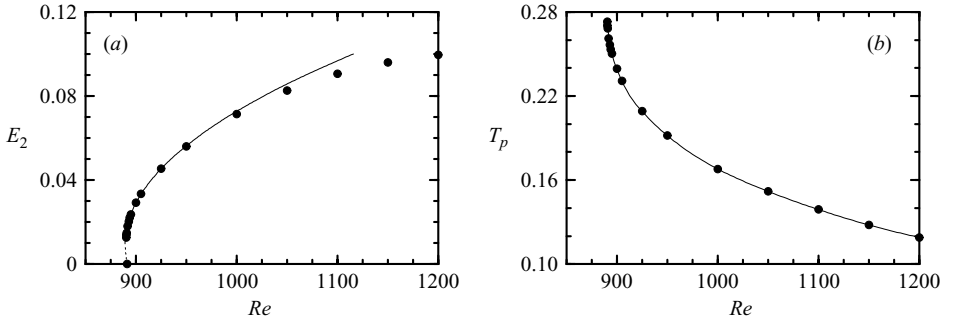

FIGURE 7. Variation with Re of (a) the amplitude squared (measured by E_2) and (b) the precession period T_p of RW2a. The curve in (a) shows the fit given by equation (4.2) and the curve in (b) is a spline fit to the data.

of the azimuthal velocity v. The jet is axisymmetric and separates the flow into two symmetric cells, as evidenced in the streamline plot. Figure 6(b) shows the corresponding contours for A1, also at $Re = 700$. The outgoing swirling jet has moved very close to the top endwall (for the symmetrically related state A1*, the jet emerges near the bottom endwall). The recirculation creates a single-cell-like flow as can be seen in the streamlines. For both A1 and N2, the jet of angular momentum erupting from the boundary layer on the rotating inner cylinder is most clearly seen in the contours of the azimuthal component of velocity v.

4. Subcritical Hopf bifurcation of A1; onset of three-dimensional states

The A1 state remains stable to $Re \approx 892$ where it suffers a subcritical Hopf bifurcation. At slightly larger Re, the flow settles into a rotating wave state with azimuthal wavenumber $m = 2$, RW2a, that precesses prograde with the rotating inner cylinder. RW2a has broken the continuous time translation Φ_τ and replaced it with a discrete time translation invariance Φ_{T_p}, where T_p is the precession period. It has also broken axisymmetry. For azimuthal wavenumber m, the flow is invariant to the cyclic group C_m, generated by the discrete rotation $R_{2\pi/m}$. For RW2a, $m = 2$ and the axisymmetry $SO(2)$ is replaced by C_2 (which is isomorphic to the abstract Z_2 group). Since RW2a is a rotating wave, time translations are equivalent to rotations:

$$\Phi_\tau(u, v, w)(r, \theta, z, t) = R_{2\pi\tau/T_p}(u, v, w)(r, \theta, z, t), \quad \tau \in \mathbb{R}. \tag{4.1}$$

RW2a has the jet emerging from the inner cylinder boundary layer near the top. Applying the K-reflection to RW2a results in another rotating wave solution state, RW2a*, with the jet emerging near the bottom.

Continuing the RW2a solution branch to lower Re, it suffers a saddle-node bifurcation at about $Re = 890.5$, so the subcriticality of the Hopf bifurcation of A1 is very slight. Figure 7(a) shows the variation with Re of E_2, a measure of the amplitude squared of RW2a. A fit to the data for $Re \leqslant 1000$ of the form

$$Re = 27,600E_2^2 - 516E_2 + 892, \tag{4.2}$$

which is the normal form for a subcritical Hopf bifurcation in terms of the amplitude squared of the oscillation, E_2, illustrates the slightly subcritical nature of the bifurcation. These results are in excellent agreement with the experimental results in Pfister *et al.* (1991) and Pfister *et al.* (1992), which report that for $\Gamma \sim 1$, A1

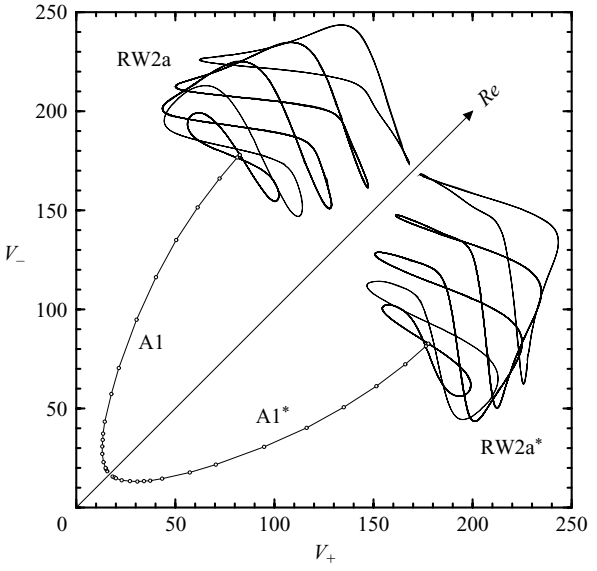

FIGURE 8. Phase portraits (V_+, V_-) of the A1, A1*, RW2a and RW2a* solution branches. The *Re* values for RW2a are 892, 925, 1000, 1100 and 1200.

suffers a Hopf bifurcation at about $Re = 880$ to a time-dependent flow with azimuthal wavenumber $m = 2$, and that for $\Gamma \leqslant 1$ this Hopf bifurcation is subcritical.

Figure 8 shows phase portraits of A1, RW2a and their symmetric complements A1* and RW2a* projected onto the plane (V_+, V_-), where $V_\pm = v(r = r_i/d + 1/2, \theta = 0, z = \pm\Gamma/4)$ are the azimuthal velocities at two symmetrically related points, at various *Re*. The portraits above the line $V_+ = V_-$ are for A1 (points) and RW2a (closed curves), while those below the line are for A1* and RW2a*. The distance from the phase portraits to the line $V_+ = V_-$ is a measure of the degree to which Z_2 symmetry is broken. The loci of A1 and A1* phase points show the supercritical pitchfork of A1 from N2 (phase points of N2 lie on the line $V_+ = V_-$), and the subcritical Hopf bifurcation from A1 to RW2a.

Figure 7(*b*) shows the variation with *Re* of the precession period T_p of RW2a. Near onset, the precession is quite slow, about 25 % of the viscous time. The figure shows that the period grows substantially as *Re* is reduced toward onset, but it remains finite. This is consistent with the experiments of Pfister *et al.* (1991) and Pfister *et al.* (1992) which report that onset of RW2a for $\Gamma > 1.1$ is via an infinite-period global bifurcation, rather than the Hopf bifurcation at lower Γ ($\Gamma \leqslant 1$).

Figure 9 shows isosurface plots of rv, the axial component of angular momentum, for RW2a at $Re = 1200$ viewed from three different perspectives. The jet emerges from the inner cylinder boundary layer near the top endwall. Its intensity varies with azimuth resulting in an $m = 2$ rotating wave whose three-dimensional structure precesses without deformation. The jet is deflected downward by the outer cylinder wall where it is concentrated into two spiral arms that are then turned in toward the inner cylinder near the bottom endwall. This causes the boundary layer on the inner cylinder to bulge. This bulge is seen to spiral up and merge with the strong jet near the top endwall.

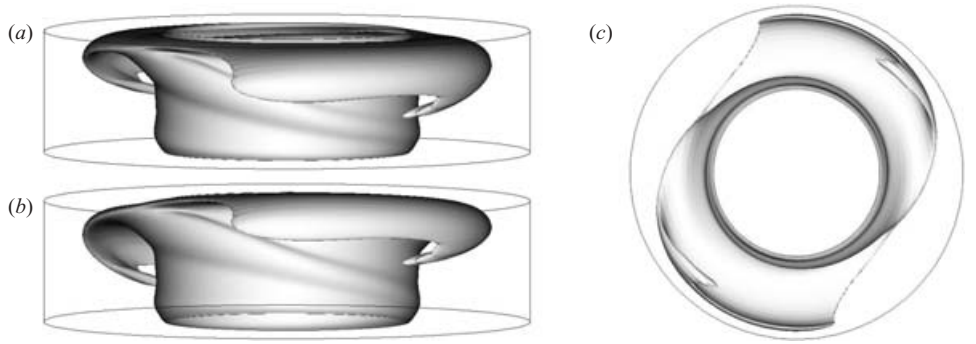

FIGURE 9. Isosurface plots of rv at level $rv = 340$ for RW2a at $Re = 1200$; view in (b) is rotated by 180° and tilted from that in (a) and (c) is the view from the bottom up.

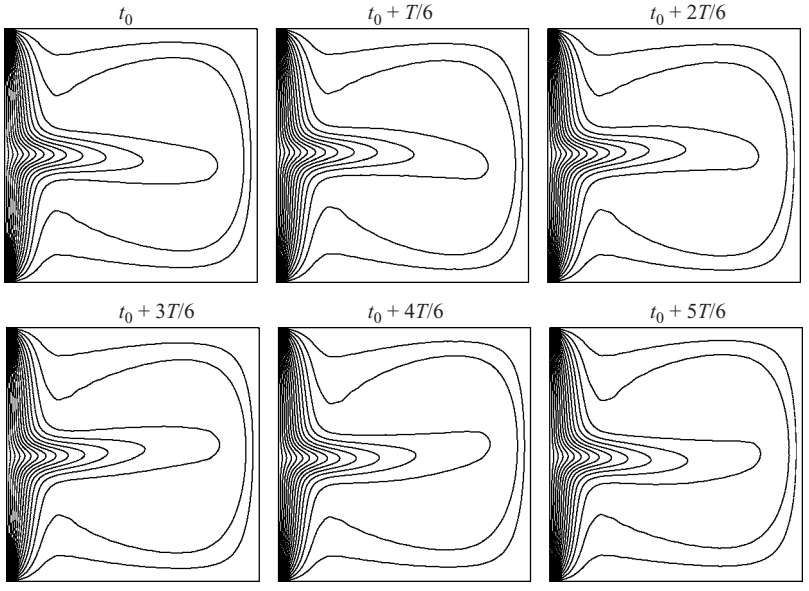

FIGURE 10. Contours of v for LC at $Re = 850$ over one period $T \approx 0.03216$. There are 16 linearly spaced contour levels in the range $v \in [0, Re]$.

The RW2a state remains stable at least to the largest Re value considered here ($Re = 1200$). We now turn our attention to the branches of solutions bifurcating from N2, where by $Re = 1200$ there are multiple three-dimensional non-periodic states.

5. Axisymmetric Hopf bifurcation of N2

At about $Re = 786$, N2 becomes unstable via a Hopf bifurcation which spawns an axisymmetric limit cycle, LC, which is invariant to the discrete time translation Φ_T, i.e. it is T-periodic. In the N2 state, the jet of angular momentum emerged from the inner cylinder boundary layer at $z = 0$ and remained symmetric about $z = 0$. For LC, the point of emergence of the jet oscillates about $z = 0$ and the jet flaps about the mid-plane so that at any instant in time, the flow is not reflection symmetric, i.e. the Z_2 symmetry generated by K has been broken. Figure 10 shows contours of v over one oscillation period of LC, illustrating the flapping of the axisymmetric jet.

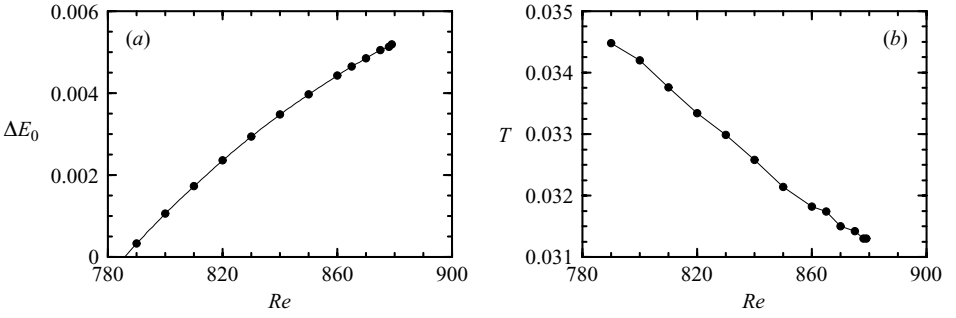

FIGURE 11. Variation with Re of (a) the amplitude squared (measured by ΔE_0) and (b) the period T of LC.

Although the flow is not K-reflection symmetric, the LC state retains a Z_2 space–time symmetry (which we denote Z_2^{ST}) generated by a reflection about $z=0$ together with a half-period temporal evolution, $K\Phi_{T/2}$ (compare the plots of LC at t and $t+3T/6$ in figure 10).

Figure 11 shows the amplitude squared (measured by ΔE_0) and the period T of LC. The linear growth of ΔE_0 with Re and the weak dependence of T on Re are typical characteristics of a supercritical Hopf bifurcation. The LC oscillations are quite fast, with small period T of about 3 % of the viscous time. Note however that T is about 40 times the rotation period of the inner cylinder ($2\pi/Re$).

At $Re\approx 880$, LC becomes unstable. For Re slightly above 880, the flow remains in a state close to LC for about one viscous time before evolving to a far-off three-dimensional time-periodic flow (described in the following section).

6. Three-dimensional states with the jet emerging about $z=0$

Using an LC state as initial condition for Re slightly above 880, the flow evolves to a rotating wave with azimuthal wavenumber $m=1$, RW1s. This is a so-called tilt wave, where the jet in N2 is tilted so that at any instant in time, RW1s is not K-reflection invariant. Figure 12 shows contours of v in various meridional planes and figure 13 is an isosurface plot of rv. As with LC, RW1s has a Z_2^{ST} space–time symmetry generated by $K\Phi_{Tp/2}$, where T_p is the precession period. But since RW1s is a rotating wave, rotation is equivalent to a temporal evolution, and so it is invariant to a spatio-temporal $SO(2)$ symmetry (denoted $SO(2)^{ST}$) generated by $R_{-\alpha}\Phi_{\alpha T_p/2\pi}$, with $\alpha\in[0,2\pi)$. Furthermore, RW1s differs from LC in that it is left invariant by a purely spatial Z_2 symmetry (which we denote Z_2^*) generated by a reflection about $z=0$ together with a π rotation around the axis, KR_π. So, the complete symmetry group of RW1s is $SO(2)^{ST}\times Z_2^*$. The invariance of RW1s to this symmetry is clearly seen in figure 12 by comparing the contour plots at θ with those (reflected through $z=0$) at $\theta+\pi$, as well as in figures 13(a) and 13(b) which are views of the isosurface from perspectives differing by 180°. Figure 13(c) clearly shows that the swirling jet forms a pair of spiral arms as it collides with the sidewall boundary layer, with one arm deflecting into the $+z$-direction and the other into the $-z$-direction. Such a pair of spirals is needed for an $m=1$ azimuthal mode with Z_2^* symmetry. A generic $m=1$ mode would only have one spiral arm.

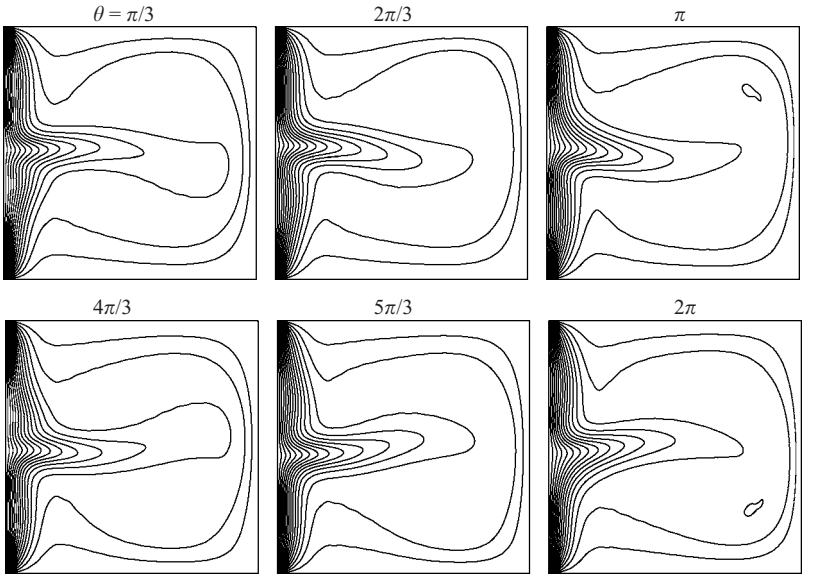

FIGURE 12. Contours of v for RW1s at $Re = 900$ in various meridional planes for θ as indicated. There are 16 linearly spaced contour levels in the range $v \in [0, Re]$.

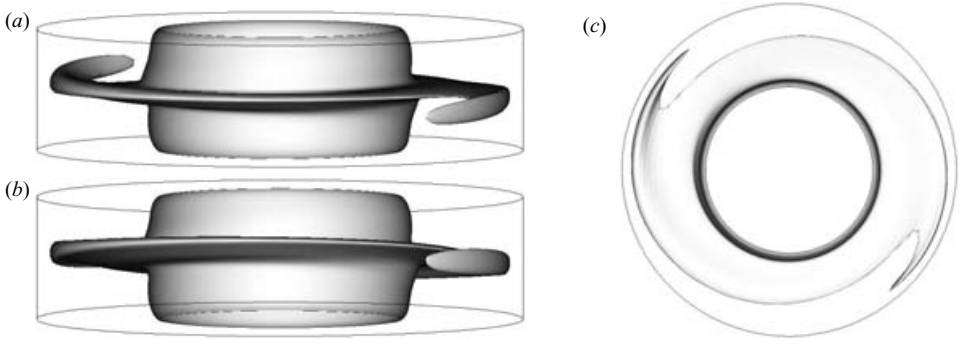

FIGURE 13. Isosurface plot of rv at level $rv = 320$ for RW1s at $Re = 900$; view in (b) is rotated by 180° and tilted from that in (a) and (c) is the view from the bottom up.

The variation with Re of the precession period of RW1s is shown in figure 14; RW1s precesses about an order of magnitude faster than RW2a, with $T_p \sim 2\,\%$ of the viscous time.

A stable RW1s is first found at $Re = 880$; attempts to continue this solution branch to lower Re result in evolutions to LC. The smallest Re at which there is a stable RW1s is 880 and the largest Re at which there is a stable LC is 879; however one cannot bifurcate directly from the other (such a bifurcation would need to be of codimension at least two, because it breaks the $SO(2)$ symmetry and simultaneously restores the Z_2 symmetry, and we are only varying Re). The characteristics of both LC and RW1s described above indicate that they both bifurcate from N2. We have only varied Re by increments of one unit, so it is possible that a succession of two Neimark–Sacker bifurcations occur in the range $Re \in (879, 880)$, one that destabilizes LC and the other stabilizes RW1s; between the two Neimark–Sacker bifurcations would exist an unstable quasi-periodic mixed-mode. This type of scenario is typical

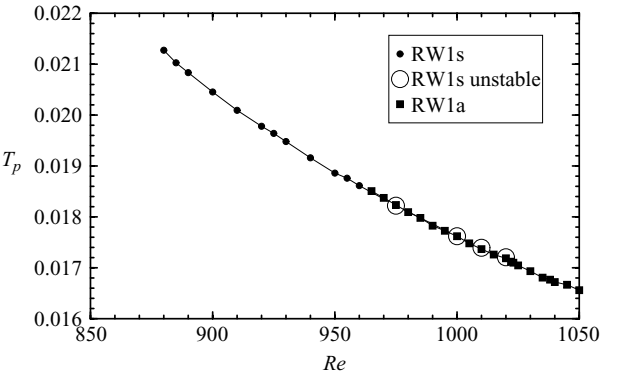

FIGURE 14. Variation with Re of the period T_p of RW1s and RW1a.

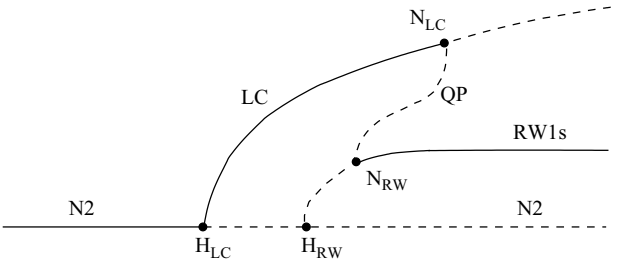

FIGURE 15. One-parameter path close to a double Hopf bifurcation, including two successive Hopf bifurcations of N2, H_{LC} and H_{RW}, two Neimark–Sacker bifurcations, N_{LC} and N_{RW}, and a quasi-periodic state QP connecting them.

of a double Hopf bifurcation. Figure 15 shows a one-parameter path close to a double Hopf bifurcation, including the aforementioned bifurcations; see Lopez & Marques (2003) for additional details. One of the Hopf bifurcations, H_{LC}, is clearly identified at $Re = 786$ where LC bifurcates from N2; the second Hopf bifurcation, H_{RW}, is estimated to occur at about $Re = 870$ by extrapolating the amplitude squared (E_1) of RW1s to zero (see figure 16). A double Hopf bifurcation of LC and RW1s has previously been found and analysed at $Re = 541$, $\Gamma = 0.5$, $\eta = 0.676$ (Lopez & Marques 2003); since the problem has three parameters, there is a one-dimensional curve of codimension-two double Hopf bifurcations. That double Hopf bifurcation and the one nearby in the present problem are probably on that curve.

RW1s remains stable up to $Re \approx 964$, at which point it suffers a supercritical pitchfork bifurcation, retaining the $SO(2)^{ST}$ but breaking the Z_2^* symmetry of RW1s, and spawns a pair of symmetrically related rotating waves, still with azimuthal wavenumber $m = 1$, RW1a and RW1a*. Figure 16(a) shows the amplitude squared of both RW1s and RW1a. We have been able to compute some unstable RW1s solutions beyond the pitchfork bifurcation either by using initial conditions close to RW1s or for Re well beyond the pitchfork bifurcation where these computed solutions were found as transient states which after some time evolve to other states to be described below. The unstable RW1s are indicated by the open symbols in the figure. The precession period of RW1a is about the same as that of RW1s; figure 14 shows the variation with Re of the precession periods of both rotating waves. Figure 17 shows

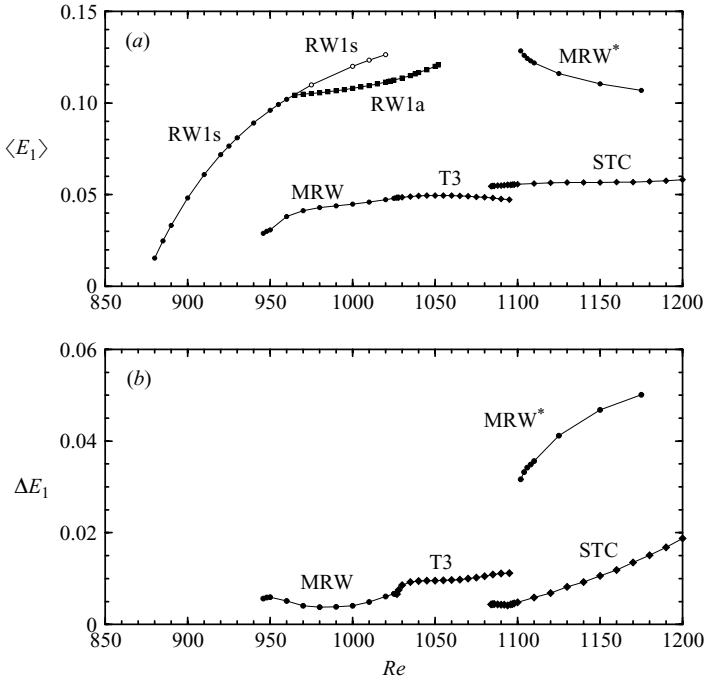

FIGURE 16. Variation with Re of (*a*) $\langle E_1 \rangle$ and (*b*) ΔE_1 of RW1s, RW1a, MRW, MRW*, T3 and STC. Open symbols in (*a*) denote unstable RW1s.

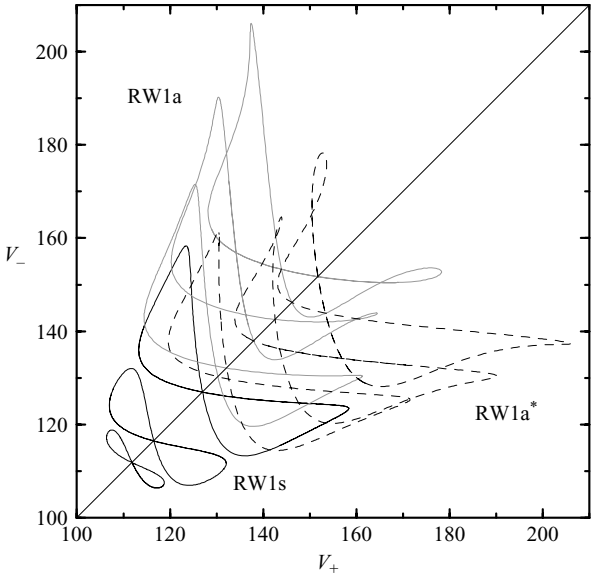

FIGURE 17. Phase portraits (V_+, V_-) of the RW1s (solid lines) and RW1a (grey dotted lines) and RW1a* (dashed lines) solution branches, over a range of Re.

phase portraits of RW1s and both RW1a and RW1a* before and after the pitchfork bifurcation. The Re values are 880, 900 and 925 for RW1s, and 970, 1010 and 1050 for RW1a. The extent to which RW1a is non-Z_2 symmetric is illustrated in the sequence

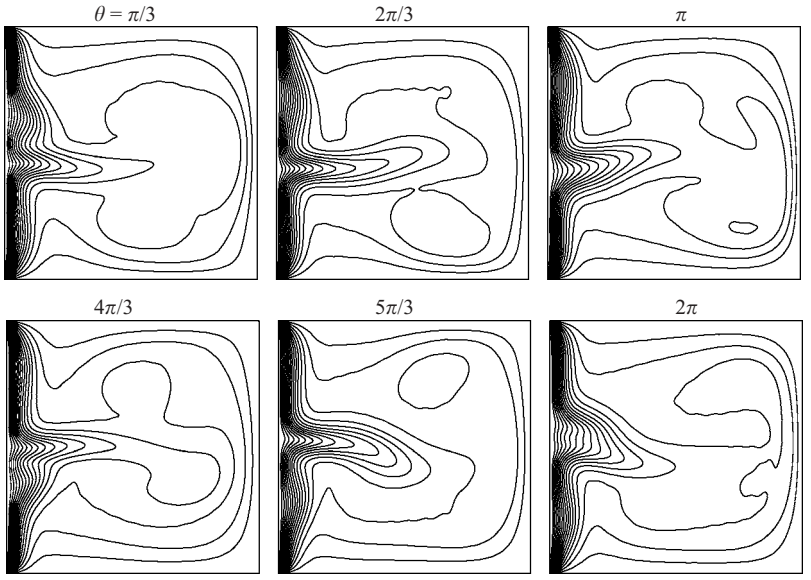

FIGURE 18. Contours of v for RW1a at $Re = 1000$ in various meridional planes for θ as indicated. There are 16 linearly spaced contour levels in the range $v \in [0, Re]$.

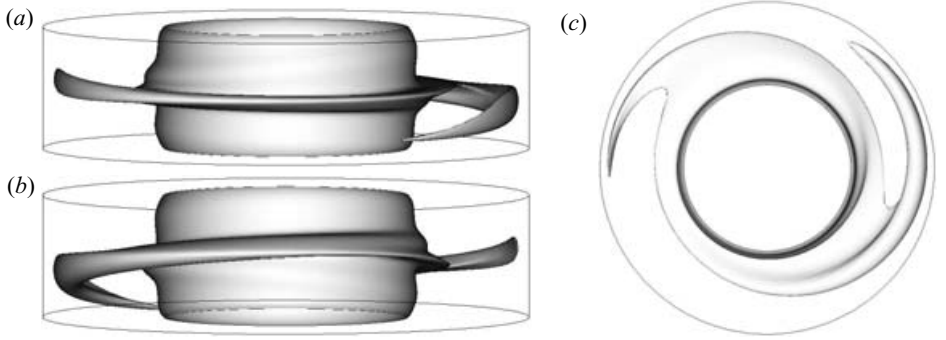

FIGURE 19. Isosurface plot of rv at level $rv = 390$ for RW1a at $Re = 1000$; view in (b) is rotated by 180° and tilted from that in (a) and (c) is the view from the bottom up.

of phase portraits in figure 17, showing the pitchfork nature of the bifurcation from RW1s to RW1a and RW1a*.

Figure 18 shows contours of v of RW1a at $Re = 1000$; the basic features are very similar to those of RW1s, the fundamental difference being that RW1a is not Z_2^* symmetric; compare contours at θ and $\theta + \pi$. The isosurface plots of RW1a in figure 19 show that as for RW1s, the jet develops two spiral arms, but now one arm is more intense than the other. Since RW1a is found at higher Re than RW1s, the boundary layer on the inner cylinder and the jet emanating from it are more intense than for RW1s. The interaction between the jet and the boundary layer on the outer cylinder wall for RW1a is quite intense and has a feedback effect on the jet at small radii. This is manifested in a spiral bulge seen in the inner cylinder boundary layer caused by the reflection of the jet from the sidewall boundary layer. This is not evident in RW1s at lower Re.

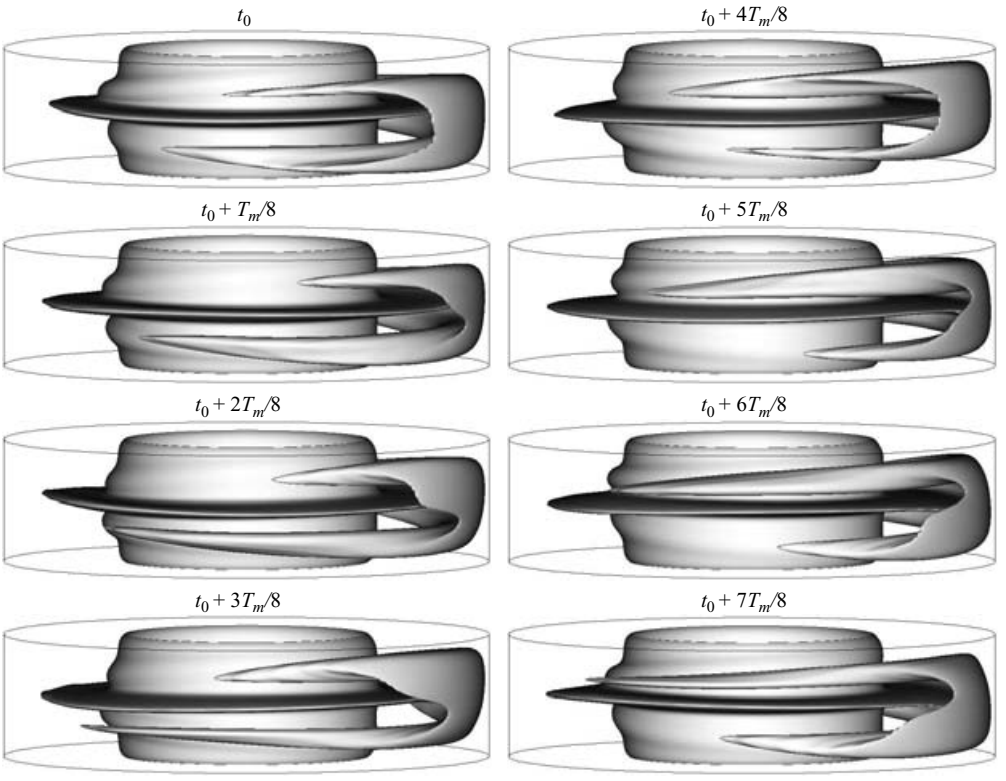

FIGURE 20. Isosurface plot of rv at level $rv = 340$ for MRW at $Re = 1025$ over one modulation period $T_m \approx 0.022$ in a frame of reference rotating with the precession period $T_p \approx 0.027$ in which MRW is a (relative) periodic orbit.

7. Transition to quasi-periodic and complex spatio-temporal dynamics

In the previous sections we have described solutions belonging to two different branches, illustrated in figure 5. The lower branch consists of A1 and RW2a, with flows consisting of singles cells that are not Z_2 symmetric. The upper branch consists of solutions exhibiting a swirling jet around $z = 0$. The solutions on the lower branch are robust, in the sense that they do not experience further bifurcations in the Reynolds number range examined (up to $Re = 1200$). In contrast, the upper branch undergoes transitions to complex dynamics in the range $1000 < Re < 1200$. How three-dimensional flows arise on both branches has been described above, and now we address the transition to complex spatio-temporal dynamics along the upper branch.

For $Re \gtrsim 950$, and coexisting with the rotating waves RW1s and RW1a, a modulated rotating wave MRW appears, as shown in figure 16. Figure 20 shows isosurfaces of rv of MRW at $Re = 1025$ over one modulation period, $T_m \approx 0.022$. The images are shown in a frame of reference rotating at the precession period of the underlying rotating wave, $T_p \approx 0.027$, in which MRW is a (relative) periodic orbit. The sequence of isosurfaces shows that the jet of angular momentum which emerges from the inner cylinder boundary layer at about $z = 0$ has a slight tilt ($m = 1$ azimuthal wavenumber), and remains coherent until it gets very close to the outer cylinder, where on one side of the cylinder it collides and spreads into the sidewall boundary layer. Due to the tilt

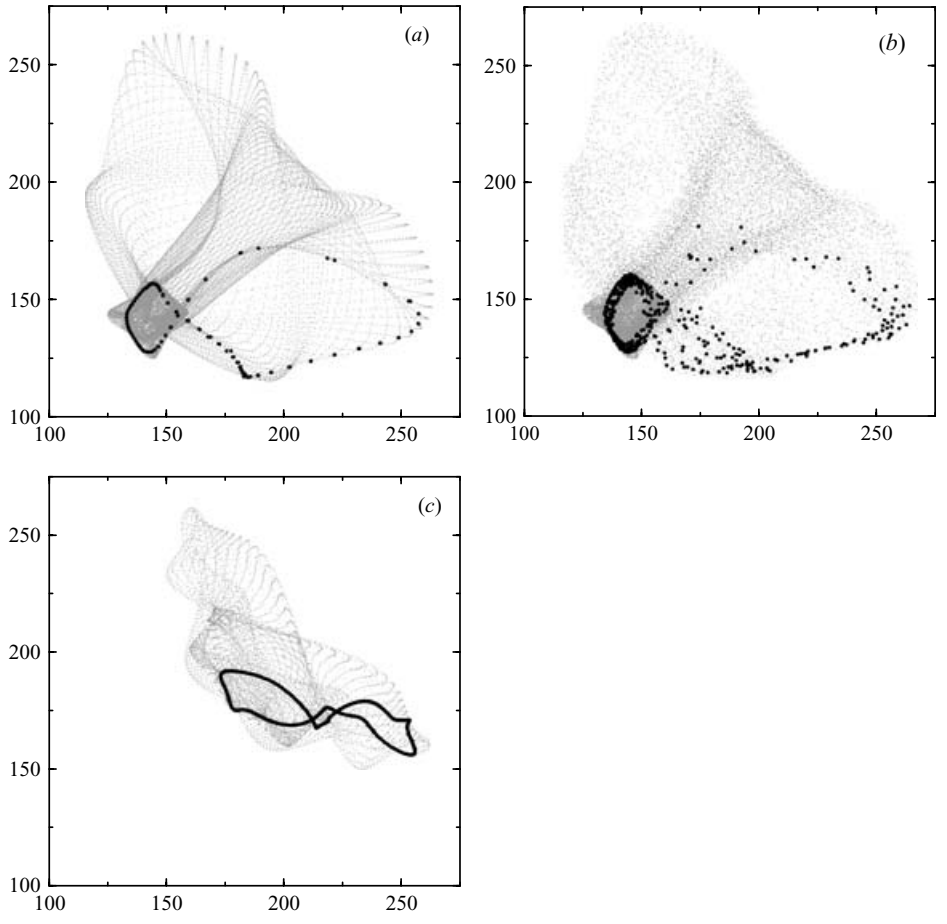

FIGURE 21. Phase portraits (V_+, V_-) (grey points) and Poincaré sections $W_+ + W_- = 0$ (black dots) of (*a*) MRW at $Re = 1025$, (*b*) T3 $Re = 1030$, and (*c*) MRW* at $Re = 1175$.

of the jet, the spreading into the sidewall layer is not symmetric about $z = 0$. However, during about half of the modulation period the jet is preferentially spread into the $+z$-direction and during the other half into the $-z$-direction. The jet of angular momentum in the sidewall boundary layer is then turned back into the interior where it spirals back into the inner cylinder boundary layer. Spiral bulges can be seen in the isosurface near the inner cylinder. The isosurface sequence also indicates that in the rotating frame, MRW has a space–time Z_2^{ST} symmetry generated by a reflection about $z = 0$ together with $T_m/2$ temporal evolution, $R_{-\pi T_m/T_p} K \Phi_{T_m/2}$. This is clearly evident by comparing the isosurface at t and $t + 4T_m/8$. This symmetry is also evident in the phase portrait (grey points) shown in figure 21(*a*) which is symmetrically distributed about the line $V_+ = V_-$. That figure also shows a Poincaré section $W_+ + W_- = 0$ drawn with larger black dots, showing a closed loop and providing clear evidence of the quasi-periodic nature of MRW. The Poincaré section cuts the 2-torus on which MRW trajectories flow twice, forming two closed loops in the section. We only show one of these in the figure.

At $Re \approx 1030$, the MRW solution changes, and complex dynamics appear. The MRW becomes a three-torus T3 at $Re \approx 1027$, as illustrated in figure 21. For T3,

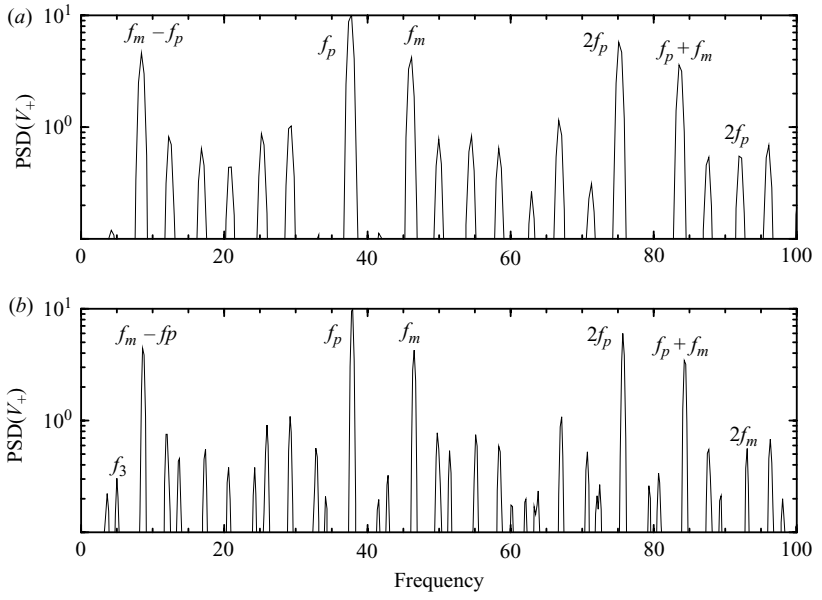

FIGURE 22. Power spectral densities of V_+ of (*a*) MRW at $Re = 1025$ and (*b*) T3 at $Re = 1030$.

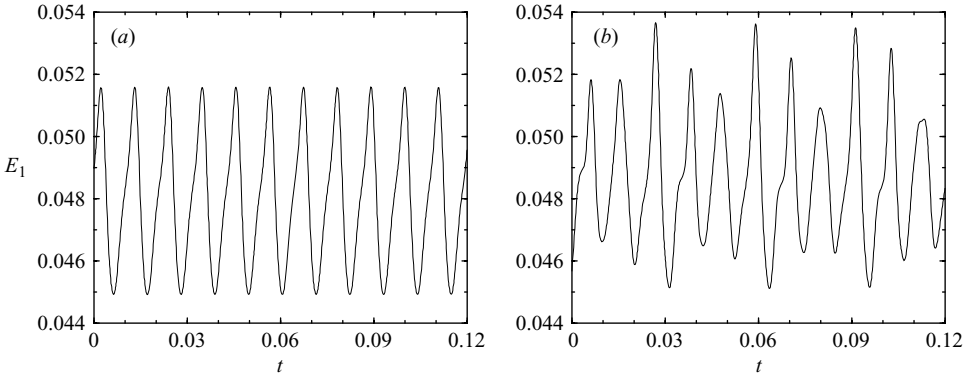

FIGURE 23. Time series of E_1 of (*a*) MRW at $Re = 1025$ and (*b*) T3 at $Re = 1030$.

all spatial and spatio-temporal symmetries of the problem have been broken. At $Re = 1025$ (figure 21*a*) the solution is still a two-torus, and the Poincaré section is a closed loop. At $Re = 1030$ (figure 21*b*) the Poincaré section is no longer a closed loop, but experiences a slow drift along the phase portrait, signalling that an additional very low frequency has appeared, and the solution is now a three-torus. Power spectrum of V_+ for MRW at $Re = 1025$ and T3 at $Re = 1030$ are shown in figure 22. The spectrum for MRW consists of peaks at the precession frequency, f_p, and at the modulation frequency, f_m, and their linear combinations, some of which are labelled in the figure. The spectrum for T3 is very similar; all of the peaks in the MRW spectrum are accounted for, but there is an additional low frequency, f_3, and its linear combinations with the other peaks. This is the third frequency of T3. Figure 23 shows short segments of the time series of the modal energy E_1 of MRW and T3. The modal energy essentially filters out the precession frequency, f_p, and for MRW $E_1(t)$ is a periodic signal with period $2/f_m$ (it is twice $1/f_m$ since E_1 is a squared

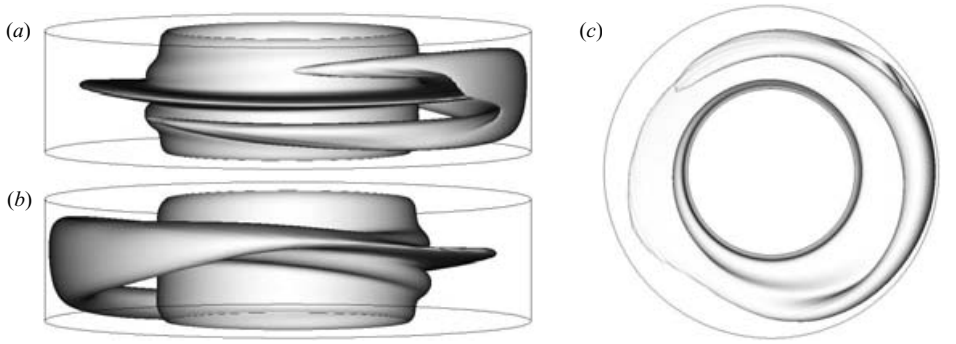

FIGURE 24. Isosurface plot of rv at level $rv = 340$ for T3 at $Re = 1030$; view in (b) is rotated by 180° and tilted from that in (a) and (c) is the view from the bottom up.

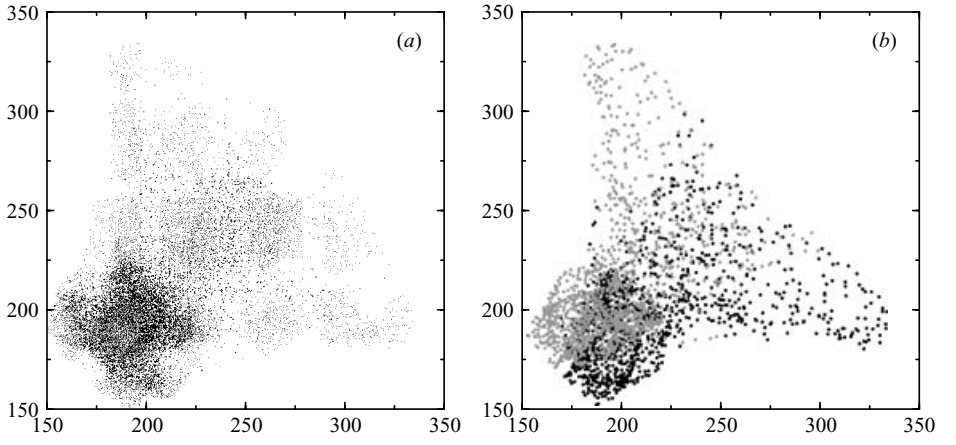

FIGURE 25. (a) Phase portrait (V_+, V_-) and (b) Poincaré section $W_+ + W_- = 0$ of STC for $Re = 1200$.

quantity). For T3, $E_1(t)$ is clearly quasi-periodic due to the presence of both f_m and f_3 frequencies.

The spatial structure of T3 is virtually indistinguishable from that of MRW; compare the isosurface plots of MRW at $Re = 1025$ in figure 20 with that of T3 at $Re = 1030$ in figure 24. The two solutions precess with about the same period, T_p (see the power spectra for the two in figure 22), and the modulation period T_m corresponding to the alternation in intensity between the spiral arm in the top half of the sidewall layer and the spiral arm in the bottom half is also common to both. The third frequency in T3 corresponds to a modulation of the relative intensification of the spiral arms such that the amount that one arm is intensified relative to the other varies on the slow f_3 time scale. This is a subtle effect, but its signature is quite evident in the E_1 time series in figure 23.

On further increasing Re, the three-torus is destroyed, and complex spatio-temporal dynamics develop. The branch of spatio-temporal complexity STC is disjoint from the T3 branch (see figure 16). The phase portrait (figure 25a) and the corresponding Poincaré section (figure 25b) for STC at $Re = 1200$ look almost identical. The STC trajectory traverses the Poincaré section in both directions; in the figure, black dots indicate intersections in one direction and grey dots are intersections in the other

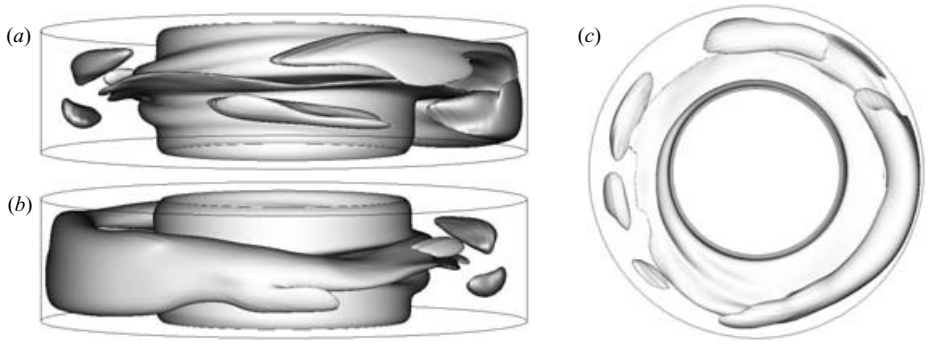

FIGURE 26. Isosurface plot of rv at level $rv = 410$ for STC at $Re = 1200$; view in (b) is rotated by 180° and tilted from that in (a) and (c) is the view from the bottom up.

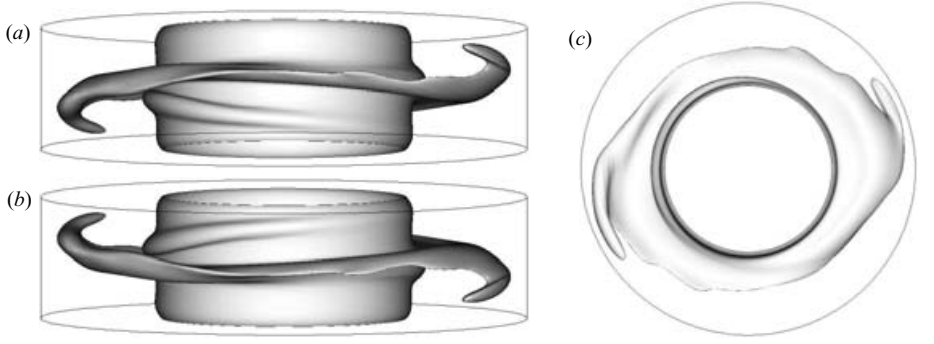

FIGURE 27. Isosurface plot of rv at level $rv = 450$ for MRW* at $Re = 1175$; view in (b) is rotated by 180° and tilted from that in (a) and (c) is the view from the bottom up.

direction. The two- and three-tori structures of MRW and T3 are destroyed and replaced by a complex attractor; all spatial and spatio-temporal symmetries are broken and the temporal coherence in T3 is also lost in STC, but both the phase portrait and Poincaré section of STC indicate that it has Z_2 symmetry in some averaged sense.

The physical structure of the STC state is not very different from that of T3; the jet still emerges from the inner cylinder boundary layer about $z = 0$ and collides with the outer cylinder boundary layer preferentially on one side since STC still has significant energy in the $m = 1$ azimuthal mode. The difference with T3 is primarily that for T3, when the jet collides with the sidewall layer, it spawns spiral arms which remain coherent, whereas for STC at higher Re the collision is more intense and the spiral arms break up. When these reflect back into the interior, they feed back onto the jet causing it to wrinkle and wobble. Figure 26 shows a snapshot isosurface of rv for STC at $Re = 1200$ from different perspectives illustrating this complex spatial structure.

At $Re \approx 1100$, a different branch of modulated rotating waves MRW* appears, as illustrated in figure 16. The phase portrait and Poincaré section of MRW* are shown in figure 21(c), clearly illustrating that this branch of quasi-periodic states is different from the others. The jet in MRW* has a pronounced $m = 1$ tilt as it emerges from the inner cylinder boundary layer near $z = 0$ and is sucked into the endwall boundary layers rather than colliding with the sidewall layer. Due to the tilt, half of the jet is sucked into the top and the other half into the bottom endwall layer. Figure 27

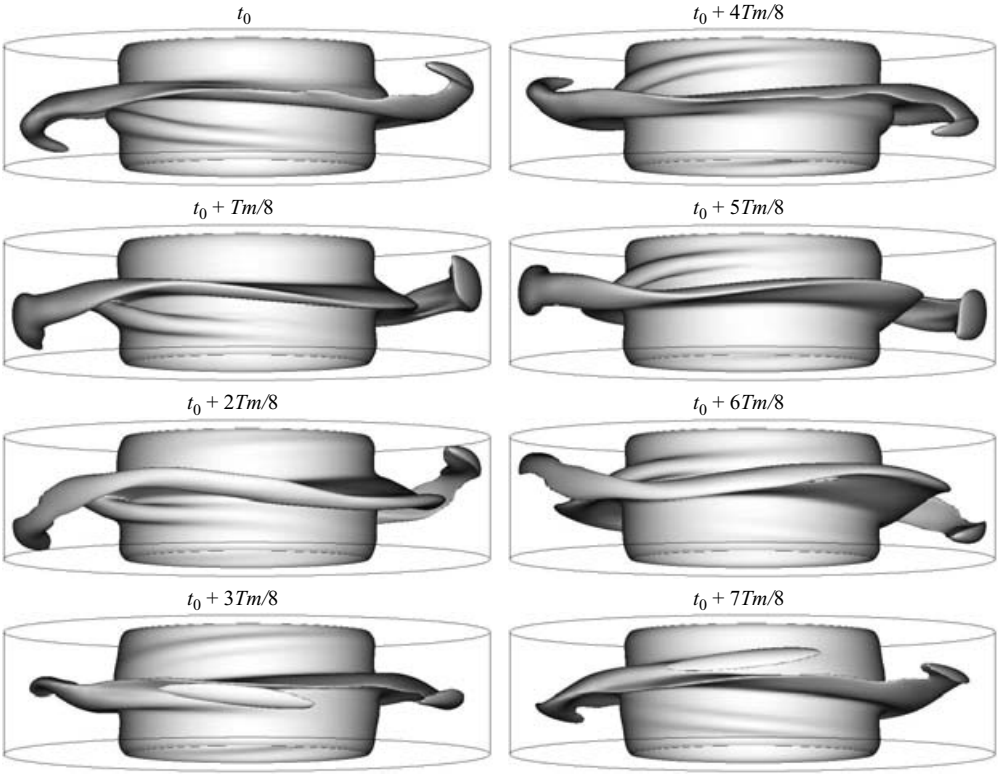

FIGURE 28. Isosurface plot of rv at level $rv = 450$ for MRW* at $Re = 1175$ over one modulation period $T_m \approx 1.44 \times 10^{-3}$ in a frame of reference rotating with the precession period $T_p \approx 0.0144$ in which MRW* is a (relative) periodic orbit.

illustrates this with an isosurface of rv at $Re = 1175$; this figure also illustrates that MRW* is invariant to the spatial Z_2^* generated by KR_π. The swirling flow in the endwall layers stretches the jet into a spiral arm in each endwall layer which snap-off periodically and the recoil in the jet is such that the part that was sucked into the top (bottom) recoils into the bottom (top) endwall layer following the snap-off. This process is illustrated in a sequence of isosurfaces of rv over one modulation period T_m, shown in figure 28 in a frame of reference rotating at the precession period T_p. It is clear that this process corresponds to a discrete spatio-temporal rotation symmetry C_2^{ST}, where in the rotating frame MRW* is invariant to a rotation R_π together with a half-period evolution $\Phi_{Tm/2}$ (compare isosurfaces at t with those at $t + 4T_m/8$). The complete symmetry group of MRW* is $C_2^{ST} \times Z_2^*$, generated by $R_{-\pi T_m/T_p} R_\pi \Phi_{T_m/2}$ and KR_π.

8. Discussion and conclusions

The onset of three-dimensional unsteady flow in the small-aspect-ratio regime of Taylor–Couette flow has been clarified. In this regime, the dynamics are dominated by the competition between the single-cell anomalous mode A1 and the two-cell normal mode N2. Whereas the steady axisymmetric aspects of this competition are well-understood following extensive experimental and numerical investigations, the onset of unsteady and three-dimensional flows observed experimentally for $Re \geqslant 800$

have presented a challenge to our understanding of their evolution, largely due to the number of competing states with both spatial and temporal complexity. Our numerical exploration in the middle of the parameter regime where this competition is manifested provides new insight into the mechanisms responsible for the onset of time-dependence and three-dimensional flow. The three-dimensional numerical solutions show that the manner in which the jet of angular momentum erupting from the inner cylinder boundary layer behaves as it redistributes the angular momentum and its interactions with the sidewall and endwall boundary layers leads to the various spatio-temporal states which break various aspects of the symmetry of the problem.

Low-dimensional dynamical systems theory has provided much guidance on and understanding of the transition processes from steady laminar flow to turbulence, inspired by works such as Ruelle & Takens (1971) and Swinney & Gollub (1981). Most studies that have focused on relating low-dimensional dynamical systems theory to transitions in fluid flows have been in geometrically simple flows, where the problem is well-defined, boundary conditions well-known, and both laboratory experiments and numerical simulations can be performed with a high degree of precision. The geometric simplicity of these problems is associated with symmetries, and it is well-known that symmetries can lead to dynamical behaviour which would be unexpected (i.e. degenerate) in the absence of symmetries (Golubitsky, Stewart & Schaeffer 1988; Crawford & Knobloch 1991; Chossat & Iooss 1994). An integral component of the present study is the implementation of dynamical systems theory and symmetry to characterize and interpret the results. Without such tools, piecing together the various solution branches and how they are related (or not) becomes a hopeless task. There is a growing wider appreciation of such an approach in hydrodynamic transitions (e.g. see the recent review by Kerswell 2005).

A summary of the various solution branches we have found, organized by their spatial and spatio-temporal symmetries and (where available) the bifurcations responsible for their birth/death is provided in figure 29. This diagram is simply a graphical summary of the stable solutions found and should not be confused with a lattice of subgroups of $SO(2) \times Z_2$ (there is an infinite number of such subgroups).

At the top of figure 29, we have the basic flow state N2, which is invariant to the full symmetry group of the problem, $SO(2) \times Z_2$, leaving the governing equations invariant. Beside each stable solution found is the symmetry subgroup leaving the solution invariant, and below each symmetry group the generators are presented. The solid downward pointing arrows correspond to the different bifurcations we have found in the present study, and each arrow is labelled with the type of bifurcation involved. The dashed arrows are conjectured connections between different solutions based on their symmetries.

The diagram (figure 29) consists of three main branches: (i) the A1 branch on which the K symmetry is broken, (ii) the STC branch along which the time invariance is broken in successive Hopf bifurcations, and (iii) a branch on which the symmetry KR_π plays an important role. The A1 branch corresponds to the states that break the reflection symmetry K, resulting in flows with the angular momentum jet emerging close to one of the endwalls. This branch is robust, in the sense that the solutions on it only undergo a Hopf bifurcation (resulting in the rotating wave state RW2a) in the Reynolds number range examined. In contrast, the solutions on the other branches experience several bifurcations resulting in complex flows; they correspond to flows with the angular momentum jet emerging from the centre of the inner cylinder. On the second branch, the K symmetry becomes a space–time symmetry of LC and MRW, and this is finally broken when all symmetries disappear in the

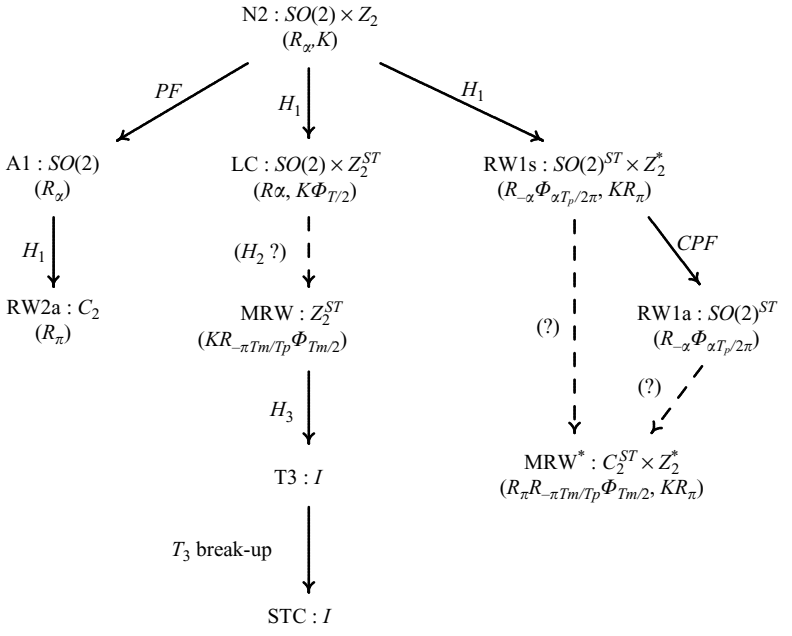

FIGURE 29. Diagram showing the relationships between the various observed solution branches, their symmetries, and the symmetry-breaking bifurcations. Bifurcations: *PF*, pitchfork; *CPF* cyclic pitchfork; H_n, Hopf bifurcation to an n-dimensional torus.

bifurcation H_3 to a three-torus state T3; the resulting symmetry group, I, contains only the identity transformation. The conjectured connection in this branch could be a Neimark–Sacker bifurcation (a Hopf bifurcation of limit cycles, H_2, resulting in a two-torus). In the third branch, all solutions except RW1a preserve the spatial symmetry KR_π, which is broken in a pitchfork bifurcation of limit cycles, *CPF*.

Our investigation has identified the modes responsible for the transition to spatio-temporal complexity. Of course, our one-parameter investigation (varying Re while keeping the geometry fixed) is incomplete in the sense that some of the bifurcations at higher Re have only been conjectured. The dynamics involved are very likely to be organized by codimension-two and codimension-three bifurcations for which a much more comprehensive study varying all three governing parameters, Re, Γ and η, is required. Such a study presents a very exciting opportunity to investigate the transition from laminar flow to spatio-temporal complexity and ultimately to turbulence in a systematic fashion in a flow where well-controlled experiments are possible.

This work was supported by the Spanish Ministry of Science and Technology grant FIS2004-01336, Spanish Ministry of Education and Science grant SAB2003-0172, and the National Science Foundation grant DMS-0509594.

REFERENCES

ABSHAGEN, J., LOPEZ, J. M., MARQUES, F. & PFISTER, G. 2005*a* Mode competition of rotating waves in reflection-symmetric Taylor–Couette flow. *J. Fluid Mech.* **538**, 269–299.

ABSHAGEN, J., LOPEZ, J. M., MARQUES, F. & PFISTER, G. 2005*b* Symmetry breaking via global bifurcations of modulated rotating waves in hydrodynamics. *Phys. Rev. Lett.* **94**, 074101.

Benjamin, T. B. 1978*a* Bifurcation phenomena in steady flows of a viscous fluid. I. Theory. *Proc. R. Soc. Lond.* A **359**, 1–26.

Benjamin, T. B. 1978*b* Bifurcation phenomena in steady flows of a viscous fluid. II. Experiments. *Proc. R. Soc. Lond.* A **359**, 27–43.

Benjamin, T. B. & Mullin, T. 1981 Anomalous modes in the Taylor experiment. *Proc. R. Soc. Lond.* A **377**, 221–249.

Chossat, P. & Iooss, G. 1994 *The Couette–Taylor Problem*. Springer.

Cliffe, K. A. 1983 Numerical calculations of two–cell and single–cell Taylor flows. *J. Fluid Mech.* **135**, 219–233.

Cliffe, K. A., Kobine, J. J. & Mullin, T. 1992 The role of anomalous modes in Taylor–Couette flow. *Phil. Trans. R. Soc. Lond.* A **439**, 341–357.

Crawford, J. D. & Knobloch, E. 1991 Symmetry and symmetry-breaking bifurcations in fluid dynamics. *Annu. Rev. Fluid Mech.* **23**, 341–387.

Furukawa, H., Watanabe, T., Toya, Y. & Nakamura, I. 2002 Flow pattern exchange in the Taylor–Couette system with a very small aspect ratio. *Phys. Rev.* E **65**, 036306.

Golubitsky, M., Stewart, I. & Schaeffer, D. G. 1988 *Singularities and Groups in Bifurcation Theory*, vol. 2. Applied Mathematical Sciences, vol. 69. Springer.

Kerswell, R. R. 2005 Recent progress in understanding the transition to turbulence in a pipe. *Nonlinearity* **18**, R17–R44.

Lopez, J. M. & Marques, F. 2003 Small aspect ratio Taylor–Couette flow: Onset of a very-low-frequency three-torus state. *Phys. Rev.* E **68**, 036302.

Lopez, J. M. & Marques, F. 2005 Finite aspect ratio Taylor–Couette flow: Shil'nikov dynamics of 2-tori. *Physica* D **211**, 168–191.

Lopez, J. M., Marques, F. & Shen, J. 2002 An efficient spectral-projection method for the Navier-Stokes equations in cylindrical geometries II. Three dimensional cases. *J. Comput. Phys.* **176**, 384–401.

Lopez, J. M., Marques, F. & Shen, J. 2004 Complex dynamics in a short annular container with rotating bottom and inner cylinder. *J. Fluid Mech.* **51**, 327–354.

Lopez, J. M. & Shen, J. 1998 An efficient spectral-projection method for the Navier-Stokes equations in cylindrical geometries I. Axisymmetric cases. *J. Comput. Phys.* **139**, 308–326.

Lorenzen, A. & Mullin, T. 1985 Anomalous modes and finite-length effects in Taylor–Couette flow. *Phys. Rev.* A **31**, 3463–3465.

Mullin, T., Toya, Y. & Tavener, S. J. 2002 Symmetry breaking and multiplicity of states in small aspect ratio Taylor–Couette flow. *Phys. Fluids* **14**, 2778–2787.

Pfister, G., Buzug, T. & Enge, N. 1992 Characterization of experimental time series from Taylor–Couette flow. *Physica* D **58**, 441–454.

Pfister, G., Schmidt, H., Cliffe, K. A. & Mullin, T. 1988 Bifurcation phenomena in Taylor–Couette flow in a very short annulus. *J. Fluid Mech.* **191**, 1–18.

Pfister, G., Schulz, A. & Lensch, B. 1991 Bifurcations and a route to chaos of an one-vortex-state in Taylor–Couette flow. *Eur. J. Mech.* B-*Fluids* **10**, 247–252.

Ruelle, D. & Takens, F. 1971 On the nature of turbulence. *Commun. Math. Phys.* **20**, 167.

Swinney, H. L. & Gollub, J. P. 1981 *Hydrodynamic Instabilities and the Transition to Turbulence*. Springer.

Taylor, G. I. 1923 Stability of a viscous liquid contained between two rotating cylinders. *Phil. Trans. R. Soc. Lond.* A **223**, 289–343.